Applied Physics A (2024) 130:564
https://doi.org/10.1007/s00339-024-07729-8

Applied Physics A
Materials Science & Processing

Enhanced ferroelectric properties of $BiFeO_3$ thin films utilizing four buffer layers: Nd_2O_3, Eu_2O_3, Ho_2O_3, and Er_2O_3

Tung-Ming Pan[1,2] · Zhong-Yi Chen[1] · Jim-Long Her[3]

Received: 11 May 2024 / Accepted: 5 July 2024 / Published online: 16 July 2024

Abstract

This paper investigates the ferroelectric and structural properties of $BiFeO_3$ thin films with four different RE_2O_3 (Nd_2O_3, Eu_2O_3, Ho_2O_3, and Er_2O_3) buffer layers fabricated on a $SrRuO_3/n^+$-Si substrate through spin-coating. To analyze the $BiFeO_3$ films with RE_2O_3 buffer layers, various techniques, such as X-ray diffraction, secondary ion mass spectrometry, atomic force microscope, and X-ray photoelectron spectroscopy were employed to investigate the crystalline structures, depth profiles, surface topographies, and chemical compositions. It was found that the $BiFeO_3$ film with RE_2O_3 buffer layers exhibited improved electrical properties such as leakage current, remnant polarization, and coercive field compared to the control $BiFeO_3$ film without a buffer layer. Moreover, the Eu_2O_3 buffer layer exhibited the lowest leakage current of 2.05×10^{-6} A/cm^2, the highest remnant polarization of 43.76 μC/cm^2, and the smallest coercive field of 188 kV/cm among all the RE_2O_3 buffer layers. The outcome is likely to have been caused by the introduction of Eu^{3+} ion to the $BiFeO_3$ film, which resulted in a reduction in surface roughness, a significant preferred orientation of (110), and an increased concentration of Fe^{3+} ion. Consequently, this inhibited the fluctuation of Fe^{3+} to Fe^{2+} ions and reduced the occurrence of oxygen vacancies.

Keywords $BiFeO_3$ · Nd_2O_3 · Eu_2O_3 · Ho_2O_3 · Er_2O_3 · Buffer layers · Sol–gel method

1 Introduction

In recent decades, $BiFeO_3$ films have garnered significant attention for their potential use in multifunctional electronic devices. This is largely due to their possession of both ferroelectricity, which occurs at a relatively high Curie temperature of approximately 830 °C, and ferromagnetism, which exhibits a high Néel temperature of around 370 °C [1–4]. Ferroelectric ABO_3 perovskites, represented by compounds such as $BaTiO_3$, $PbZr_{0.53}Ti_{0.47}O_3$, $SrTiO_3$, and $LaAlO_3$ [5–7], are highly regarded materials recognized for their unique perovskite crystal structure. This structure is characterized by A-site cations at the corners, B-site cations at the center, and a surrounding network of oxygen anions. Typically represented by the formula ABX_3, where A and B are cations and X is an anion, commonly oxygen [8–10]. $BiFeO_3$ stands out among ferroelectric materials due to its exceptional combination of multiferroic properties, high Curie temperature, chemical durability, robust piezoelectricity, and tunable characteristics. These attributes make $BiFeO_3$ a highly promising material for a wide range of technological applications, including spintronics, sensors, actuators, data storage, and energy conversion devices [11–13].

The presence of active lone-pair electrons in $BiFeO_3$ is believed to generate ferroelectric polarization, as the $6s^2$ orbitals electrons fill one of the resulting orbitals in the Bi^{3+} ion (A site). In contrast to its magnetic property, the superexchange interactions of Fe^{3+} (B site) and O^{2-} ions result in antiferromagnetic behavior with G-type magnetic ordering [14]. However, the twisted rhombohedral perovskite structure of the $BiFeO_3$ film, which belongs to the R3c space group, exhibits a large leakage current and high coercive field [15, 16], limiting its potential applications. Researchers have pursued approaches such as ion substitution, process modification, and insertion of a buffer layer to overcome these limitations.

✉ Tung-Ming Pan
tmpan@mail.cgu.edu.tw

[1] Department of Electronics Engineering, Chang Gung University, Taoyuan 33302, Taiwan, ROC

[2] Division of Urology, Linkou Medical Center, Chang Gung Memorial Hospital, Taoyuan 33305, Taiwan, ROC

[3] Division of Natural Science, Center for General Education, Chang Gung University, Taoyuan 33302, Taiwan, ROC

Incorporating transition and rare-earth (RE) metals into $BiFeO_3$ films has been suggested as a means to enhance leakage current performance. By substituting RE ions for Bi ions at the A site and transition ions for Fe ions at the B site, the loss of Bi^{3+} ions can be prevented, and fluctuations in the valence state of Fe^{3+} ions can be inhibited. Consequently, these actions may increase intrinsic polarization and decrease leakage current levels [1, 17–20]. Nevertheless, doping $BiFeO_3$ films with RE elements presents various challenges, including concerns regarding phase stability, fluctuations in charge carrier concentration, structural integrity, thermal behavior, uneven distribution of dopants, fabrication complexities, and compatibility issues during integration [21, 22]. Doping perovskites with RE ions results in the charge compensation, either through the formation of oxygen vacancies or alterations in the oxidation states of other cations in the compound. These vacancies significantly impact the structural, electronic, and functional properties of the film [23–25]. Additionally, the Bi layer-structured ferroelectrics play a crucial role in determining the electrical properties of these materials, significantly influencing ferroelectricity, dielectric behavior, piezoelectricity, conductivity, multiferroicity, thermal stability, and fatigue resistance [26, 27].

Several research teams have observed significant impacts on the characteristics of $BiFeO_3$ thin films based on the chosen buffer layer. Specifically, Zheng et al. noted that employing a $SrRuO_3$ buffer layer led to improved electrical properties of the $BiFeO_3$ thin film due to enhancements in surface morphology and crystallization [28]. Leu et al. demonstrated that the addition of a Bi_2O_3 buffer layer effectively bolstered both the structural and electrical properties of the $BiFeO_3$ thin film [29]. Similarly, Tang et al. reported that the use of $LaNiO_3$ as a buffer layer enhanced the crystalline quality of $BiFeO_3$, as it is structurally compatible with $BiFeO_3$ [30]. Finally, Cao et al. provided evidence that La^{3+}-doped $BiFeO_3$ films deposited on Si substrates with $LaNiO_3$ as a buffer layer displayed a pronounced magneto-optical effect [31]. Additionally, research has explored the incorporation of RE ions into the CdSe or CdS films. The inclusion of Er in CdSe nanocrystals leads to notable changes in the lattice structure of $Cd_{1-x}Er_xSe$, thereby enhancing photoluminescence [32]. Furthermore, studies have examined the structural and optical properties of $Cd_{1-x}Eu_xS$ thin films fabricated on glass through a chemical bath method [33].

Sol–gel spin-coating was selected for its versatility in depositing a range of materials, including oxides, nitrides, and composites. It is suitable for creating complex multilayer structures and heterostructures. This method produces uniform, high-quality thin films with precise compositional control, offering cost-effectiveness and scalability while allowing fine-tuning of film properties and morphology [34–36]. In this study, RE_2O_3 film is selected as the buffer layer for various reasons: (1) RE_2O_3 film possesses large energy gap, high dielectric constant and good thermal stability; (2) RE cations can be substituted for the Bi^{3+} ion in the $BiFeO_3$ film to modify the crystal structure; (3) RE_2O_3 film can act like a sink for defects or oxygen vacancies in the buffer layer; and finally, (4) RE_2O_3 film can hinder the electron injection from the bottom electrode. The present investigation delves into the production of $BiFeO_3$ thin films using a sol–gel spin-coating technique that operates at a low temperature. This process may be appropriate for Si process technology. The current literature lacks investigation of the ferroelectric behavior of $BiFeO_3$ thin film on different RE_2O_3 buffer layers (Nd_2O_3, Eu_2O_3, Ho_2O_3, and Er_2O_3), and this research topic addresses this gap. The study focuses on the structural, surface morphological, depth profiles, film compositional, and ferroelectric properties of $BiFeO_3$ thin films with and without RE_2O_3 buffer layer on $SrRuO_3$. The results demonstrate that the incorporation of RE_2O_3 films as a buffer layer can reduce leakage current and improve remanent polarization.

2 Experimental

Strontium nitrate $Sr(NO_3)_2$ and ruthenium chloride hydrate $RuCl_3{\cdot}xH_2O$ were utilized as the primary raw materials for synthesizing $SrRuO_3$ film. Meanwhile, bismuth nitrate pentahydrate $Bi(NO_3)_3{\cdot}5H_2O$ and iron nitrate $Fe(NO_3)_3{\cdot}9H_2O$ were utilized for $BiFeO_3$ thin film synthesis. In addition, neodymium acetate hydrate $Nd(CH_3CO_2)_3{\cdot}xH_2O$, europium acetate hydrate $Eu(CH_3CO_2)_3{\cdot}xH_2O$, holmium acetate hydrate $Ho(CH_3CO_2)_3{\cdot}xH_2O$, and erbium acetate hydrate $Er(CH_3CO_2)_3{\cdot}xH_2O$ were used for synthesizing different RE_2O_3 buffer layers such as Nd_2O_3, Eu_2O_3, Ho_2O_3, and Er_2O_3. The chemical reagents were obtained from Sigma Aldrich and were combined in a specific ratio. For instance, $BiFeO_3$ was prepared using a 1:1 ratio of bismuth and iron nitrates with an additional 10% weight of bismuth nitrate to account for losses during the sol–gel process, while $SrRuO_3$ was prepared using a 1:1 ratio of strontium nitrate and ruthenium chloride hydrate.

To produce a high-quality precursor solution, a 1:1 mixture of 0.1 M strontium nitrate and 0.1 M ruthenium chloride hydrate was dissolved in 10 mL of ethanol. Separately, 0.25 M bismuth nitrate and 0.2 M iron nitrate were dissolved in 10 mL of ethylene glycol with constant stirring. The two solutions were then combined and stirred at 70 °C for 2 h. Citric acid was added as a stabilizer to adjust the solution's viscosity during gel formation. Next, 0.1 M neodymium acetate hydrate, 0.1 M europium acetate hydrate, 0.1 M holmium acetate hydrate, or 0.1 M erbium acetate hydrate was dissolved in 10 mL of nitric acid and stirred for 2 h. Citric

acid was used as a complexing agent to stabilize the metal-citrate complex in aqueous solutions.

First, the $SrRuO_3$ gel was spin-coated onto an n^+-silicon (100) substrate at 200 rpm for 30 s, followed by 1000 rpm for 15 s. The substrate was heated on a hot plate at 200 °C for 3 min and annealed in N_2 gas at 550 °C for 1 h. Next, the RE_2O_3 (Nd_2O_3, Eu_2O_3, Ho_2O_3, and Er_2O_3) chemical solutions were spin-coated on the $SrRuO_3/n^+$-Si substrate at 200 rpm for 10 s, followed by 2000 rpm for 20 s. The substrates were baked on a hot plate at 150 °C for 3 min and annealed in O_2 gas at 400 °C for 10 min. Subsequently, thin $BiFeO_3$ films were spin-coated onto the RE_2O_3 buffer layers at 200 rpm for 10 s, followed by 3000 rpm for 20 s. These films were baked on a hot plate at 200 °C for 3 min and then annealed in O_2 gas at 400 °C for 10 min. Finally, all $BiFeO_3/RE_2O_3/SrRuO_3/n^+$-Si substrate thin films were annealed at 600 °C for 1 h, and 50 nm-thick Pt top electrodes were deposited using a sputtering system with an area of 3.14×10^{-4} cm^2 through a shadow mask. Figure 1a and b illustrate the schematic cross-sectional views of the $BiFeO_3$ film and the RE_2O_3-buffered $BiFeO_3$ film, respectively.

The $BiFeO_3$ thin films with four different RE_2O_3 buffer layers were analyzed for their structural characteristics using various techniques, including X-ray diffraction (XRD), atomic force microscopy (AFM), X-ray photoelectron spectroscopy (XPS), and secondary ion mass spectrometry (SIMS). The crystallographic measurements were performed using a Rigaku D/MAX2000 XRD with a radiation wavelength (λ) of 1.5418 Å and a 2θ range of 10–90°, with a step size of 0.04°/s. The surface topography of the films was examined with a Solver P47-PRO SPM in tapping mode, and the surface roughness was determined from 3×3 μm^2 scan areas. The depth profiles of the films were analyzed using a ToF–SIMS IV/Ion-Tof system with an O_2^+ primary beam. The chemical bonding of the $BiFeO_3$ films with different RE_2O_3 buffer layers was investigated using a Thermo Scientific ESCALAB XI^+ X-ray photoelectron spectrometer microscope. The leakage current density–electric field (J–E) characteristics and polarization–electric field (P–E) hysteresis loops of the $BiFeO_3$ thin films were measured using a Keysight B1500A semiconductor device analyzer and a modified Sawyer–Tower circuit, respectively, for each of the four RE_2O_3 buffer layers.

3 Results and discussion

3.1 Structural properties of $BiFeO_3$ with four RE_2O_3 buffer layers

The XRD patterns in Fig. 2a depict the $BiFeO_3$ thin films with and without various RE_2O_3 buffer layers. The primary diffraction peak, indexed as a hexagonal $BiFeO_3$ structure with R3c space group [JCPDS: 71-2494], was observed in the control sample at (202). However, the formation of impurity and secondary phases is a common occurrence in the synthesis of $BiFeO_3$ films using solid-state and sol–gel methods, primarily due to imprecise temperature control

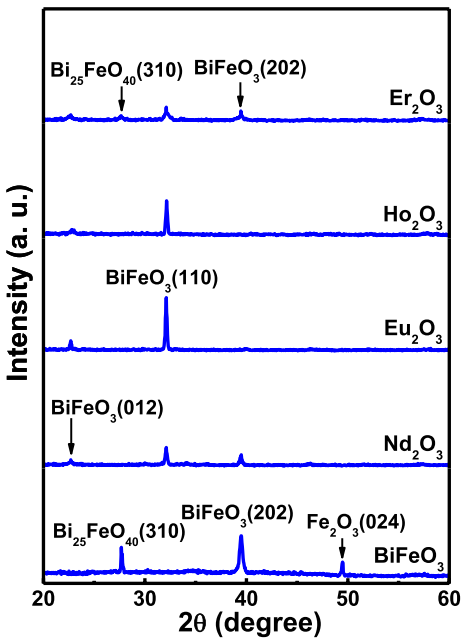

Fig. 2 XRD patterns of $BiFeO_3$ thin film and four different RE_2O_3-buffered $BiFeO_3$ films

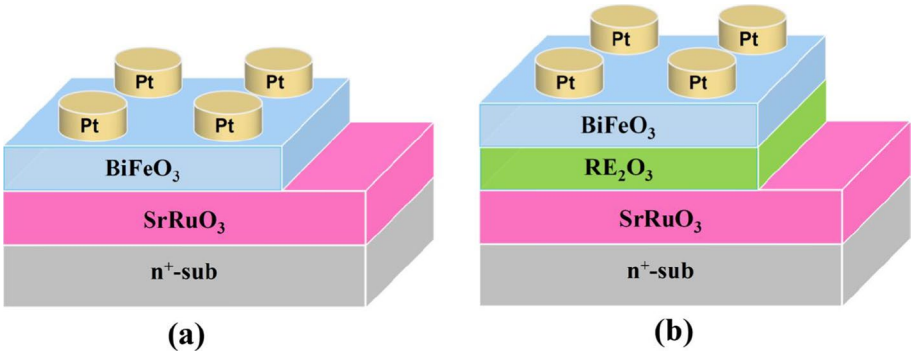

Fig. 1 Schematic cross-section views of capacitive device structures using **a** $BiFeO_3$ and **b** RE_2O_3-buffered $BiFeO_3$ films

[37, 38]. The XRD analysis revealed the prominent $BiFeO_3$ (202) peak, accompanied by impurities (Fe_2O_3) and secondary phases ($Bi_{25}FeO_{40}$) [JCPDS: 33-0664 and 46-0416] present in the control sample. This contrasts with the findings of Zheng et al. [39] and Wu and Wang [40], who observed strong preferred $BiFeO_3$ (110) and notable (111) orientations, respectively, in their thin films. With the substrate temperature increasing from 450 to 620 °C, the overall crystallinity of the $BiFeO_3$ film significantly improved, as evidenced by the enhanced sharpness and peak intensity of the (111) peak in the XRD patterns. In the $BiFeO_3$ films with the RE_2O_3 buffer layer, a more distinct $BiFeO_3$ (110) peak was observed, while it was absent in the film lacking the RE_2O_3 buffer layer. The addition of the RE buffer layer prompted the formation of a single-phase $BiFeO_3$ structure during annealing at 600 °C, with RE ions occupying the A site within the crystal lattice, as verified by SIMS data. This process effectively eradicated the presence of multiple phases. This behavior can be ascribed to the smaller ionic radii of Nd^{3+} (0.983 Å), Eu^{3+} (0.947 Å), and Ho^{3+} (0.901 Å) ions in comparison to Bi^{3+} (1.03 Å) ions [41]. In the sample featuring an Er_2O_3 buffer layer, three faint $BiFeO_3$ diffraction peaks were observed, suggesting a distorted pervoskite-based hexagonal structure, accompanied by a relatively weak (310) peak corresponding to the $Bi_{25}FeO_{40}$ secondary phase. However, these impurity and secondary phase peaks vanished in the Nd_2O_3, Eu_2O_3, and Ho_2O_3-buffered $SrRuO_3$ film, indicating the integration of trivalent Nd, Eu, and Ho ions into the $BiFeO_3$ crystal lattice. The $BiFeO_3$ film with the Nd_2O_3 buffer layer exhibited three faint peak intensities, while those with the Eu_2O_3 and Ho_2O_3 buffer layers showed two distinct diffraction peaks at 22.74 ~ 22.82 and 32.12 ~ 32.20 corresponding to (012) and (110). Additionally, the $BiFeO_3$ films with the Nd_2O_3, Eu_2O_3, and Ho_2O_3 buffer layers demonstrated characteristic peaks slightly shifted towards higher diffraction angles. The introduction of RE elements aided in reducing oxygen vacancies and suppressing the formation of impurity phases associated with the oxidational states of Fe^{3+} [20], without inducing any structural transitions.

SIMS analysis was employed to examine the influence of the RE_2O_3 buffer layer on the depth distributions of elements across the thickness of $BiFeO_3$ thin films. Figure 3a gives that the distribution of Bi and Fe in the $BiFeO_3$ film was uniform, except at the interface with the $SrRuO_3$ electrode, where a notable decrease in Fe and Bi concentrations occurred. This implies significant inward diffusion of Fe and Bi ions at the $SrRuO_3$/Si interface, consistent with previous research [42] that emphasizes substantial inward diffusion of Bi and Fe into the Si substrate in SIMS profiles. The presence of an RE_2O_3 buffer layer notably affects the distribution of elements in the $BiFeO_3$ thin film. Figure 3b–e show that the Bi ion intensities in samples with various RE_2O_3 buffer layers were higher than in the control sample, indicating different crystallinity. This outcome can be attributed to the elevated concentration of Bi, which accelerates volatile or out-diffusion of Bi from the unstable buffer layer, leading to the formation of a defective film structure. Moreover, a small amount of RE ions in the buffer layer diffused gradually and incorporated into the $BiFeO_3$, resulting in a consistently high concentration of Bi. While the samples with different RE_2O_3 buffer layers exhibited distinct properties, their distributions of Bi and Fe elements were similar. It was observed that the Bi ions accumulated in the $SrRuO_3$ film, except for the Ho_2O_3 buffer layer. The RE buffer layers not only facilitated the formation of the (110) orientation but also hindered the crystallization of Bi-rich phases. Moreover, there was minor inter-diffusion between $BiFeO_3$ and RE_2O_3 due to the low deposition temperature of the $BiFeO_3$ film. The sample featuring the Eu_2O_3 buffer layer exhibited the highest Bi ion intensity, likely due to the incorporation of Eu ions into the $BiFeO_3$ film, which suppressed the out-diffusion of Bi ions. Conversely, the Er_2O_3 buffer layer facilitated a localized high Bi concentration, enhancing $BiFeO_3$ crystallization; however, its instability resulted in the formation of a structurally defective film with a Bi-depleted surface. Thus, we suggest employing $BiFeO_3$ thin films with RE_2O_3 buffer layers, as they facilitate the nucleation and growth of the (110) texture structure with reduced lattice distortions.

Figure 4 depicts the surface morphologies of $BiFeO_3$ thin films examined using AFM with and without various RE_2O_3. The control $BiFeO_3$ film had a surface roughness of 12.6 nm, while films with Nd_2O_3, Eu_2O_3, Ho_2O_3, and Er_2O_3 buffer layers showed roughness values of 7.67, 5.77, 6.97, and 8.56 nm, respectively. In contrast, the $BiFeO_3$ film deposited on the $SrRuO_3$ electrode had an uneven, flaky, and micro-cracked surface. However, the use of RE_2O_3 buffer layers resulted in notable differences in surface morphology, with flatter surfaces and smaller grain sizes observed in the RE_2O_3 buffered-$BiFeO_3$ films. The presence of minor grains in the $BiFeO_3$ films on the RE_2O_3 buffer layer is attributed to the high number of nucleation sites in the buffer layer, resulting in lower R_{rms} values. It is noteworthy that the RE_2O_3 buffer layer visibly improved the surface morphology by smoothing it out, with reduced size and number of hills when Bi is substituted by RE ions. The bond energy of RE–O is stronger than those of Fe–O and Bi-O, as per the Pauling electronegativity concept. The electronegativity values of Bi, Fe, Nd, Eu, Ho, Er, and O are 2.02, 1.83, 1.14, 1.2, 1.23, 1.24, and 3.44, respectively. Consequently, more formation heat is expelled during film growth, leading to a more stable structure.

To comprehend the ferroelectric characteristics of $BiFeO_3$ films, it is essential to assess the variable oxidation state of Fe ions between Fe^{2+} and Fe^{3+}, which significantly influences the properties of the film. To achieve this,

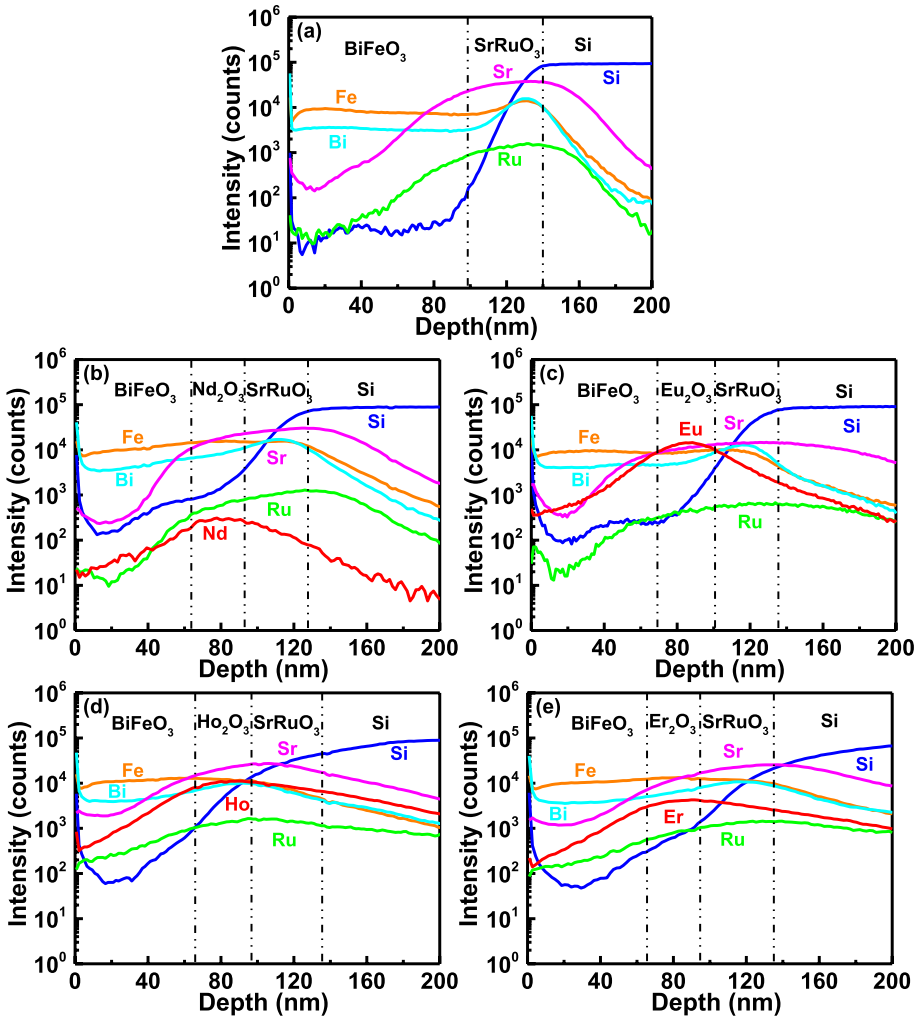

Fig. 3 SIMS depth profile of **a** control $BiFeO_3$ film and that with **b** Nd_2O_3, **c** Eu_2O_3, **d** Ho_2O_3, and **e** Er_2O_3 buffer layers

the oxidation states of Fe ions in control $BiFeO_3$ films and RE_2O_3-buffered $BiFeO_3$ films were assessed by analyzing the narrow scan XPS spectra of Bi 4f, Fe 2p, and O 1 s lines, as shown in Fig. 5a–c. The calibration of the core-level photoelectron binding energies was achieved by using the binding energy of the C 1 s photoelectron at 285 eV. Following the subtraction of the Shirley-type background, the spectra were deconvoluted using Gaussian-Lorentz functions. The Bi doublet in the spectrum of the control sample consisted of two peaks at 159.1 and 164.4 eV, with a spin–orbit splitting of 5.3 eV, attributed to the Bi-O bonds. The RE_2O_3 buffer layer caused a slight shift in the Bi $4f_{7/2}$ and Bi $4f_{5/2}$ peaks towards higher binding energies (0.1 ~ 0.2 eV), indicating substitution of RE^{3+} ions at Bi^{3+} sites in the $BiFeO_3$ lattice. The chemical shift in Bi 4f two peaks may be due to the variation in electronegativity values of the elements Bi, Fe, Nd, Eu, Ho, Er, and O. The covalency/ionicity of Bi–O, Fe–O, Nd–O, Eu–O, Ho–O, and Er–O bonds were calculated for the samples with and without the RE_2O_3 buffer layer. The fraction of covalency (F_c) was defined as $F_c = \exp(-(\Delta E_N)^2/4)$, where ΔE_N is the difference in electronegativity value between the anion and cation, while the fraction of ionicity was estimated by $F_i = (1 - F_c)$ [43]. Based on the electronegativity values of Bi, Fe, Nd, Eu, Ho, Er, and O elements mentioned above, the F_c values of Bi–O, Fe–O, Nd–O, Eu–O, Ho–O, and Er–O bonds were calculated to be 0.6, 0.52, 0.27, 0.29, 0.29, and 0.3, respectively, while those of Fi values were estimated to be 0.4, 0.48, 0.73, 0.71, 0.71, and 0.7. The ionicity value of the RE–O bond is much greater than that of the Bi–O bond, suggesting that the bonding energy of the RE–O bond in the oxygen octahedron is higher than that of the Bi–O bond, leading to a slight shift of the $4f_{7/2}$ and Bi $4f_{5/2}$ peaks towards higher binding energies.

The Fe 2p XPS core spectra for the control $BiFeO_3$ sample and $BiFeO_3$ samples with RE_2O_3 buffer layers are presented in Fig. 5b. The peaks at ~ 710.1 and ~ 723.8 eV were observed for Fe^{3+} oxidation state, while those at ~ 712.1 and ~ 726 eV were assigned to Fe^{2+} oxidation state [44]. Additionally, satellite peaks for $2p_{3/2}$ and $2p_{1/2}$ were observed at ~ 718.5 and ~ 732.1 eV, respectively, which are characteristic of the Fe oxidation state. The compositional ratio of Fe^{2+}/Fe^{3+} was calculated as 0.98, 0.87, 0.74, 0.84

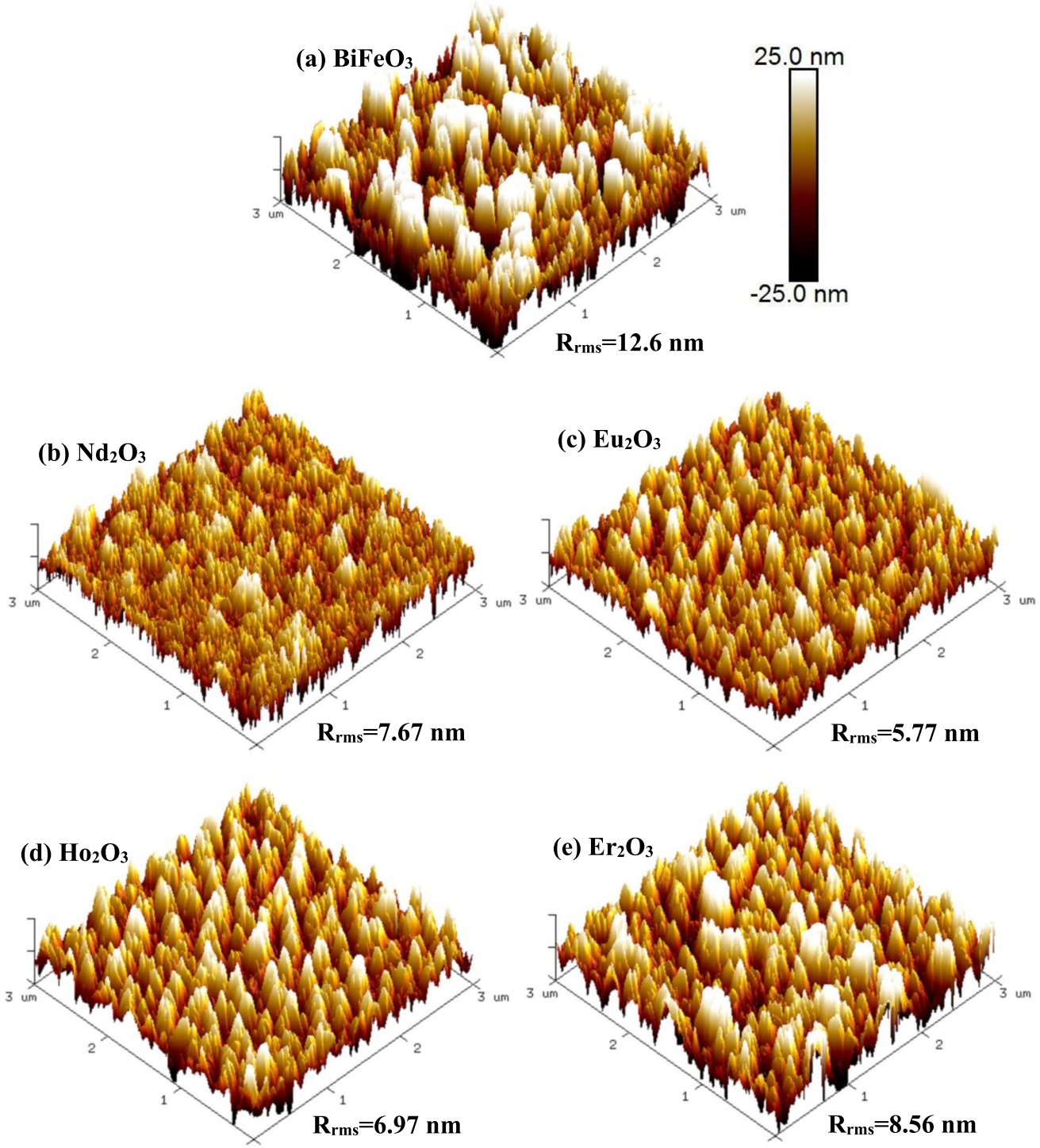

Fig. 4 AFM images of **a** control $BiFeO_3$ film and $BiFeO_3$ film with **b** Nd_2O_3, **c** Eu_2O_3, **d** Ho_2O_3, and **e** Er_2O_3 buffer layers

and 0.91 for the control $BiFeO_3$ sample and those with Nd_2O_3, Eu_2O_3, Ho_2O_3, and Er_2O_3 buffer layers, respectively, using curve fitting. The $BiFeO_3$ samples with RE_2O_3 buffer layers showed a lower Fe^{2+}/Fe^{3+} compositional ratio compared to the control sample. The Eu_2O_3-buffered $BiFeO_3$ film demonstrated the lowest compositional ratio among the buffer layers, possibly due to the incorporation of Eu^{3+} ion, which enhances the crystallization behavior of $BiFeO_3$, suppresses the volatilization of Bi^{3+} ion, and reduces the oxygen vacancy. Figure 5c gives the de-convoluted O 1 s peak into

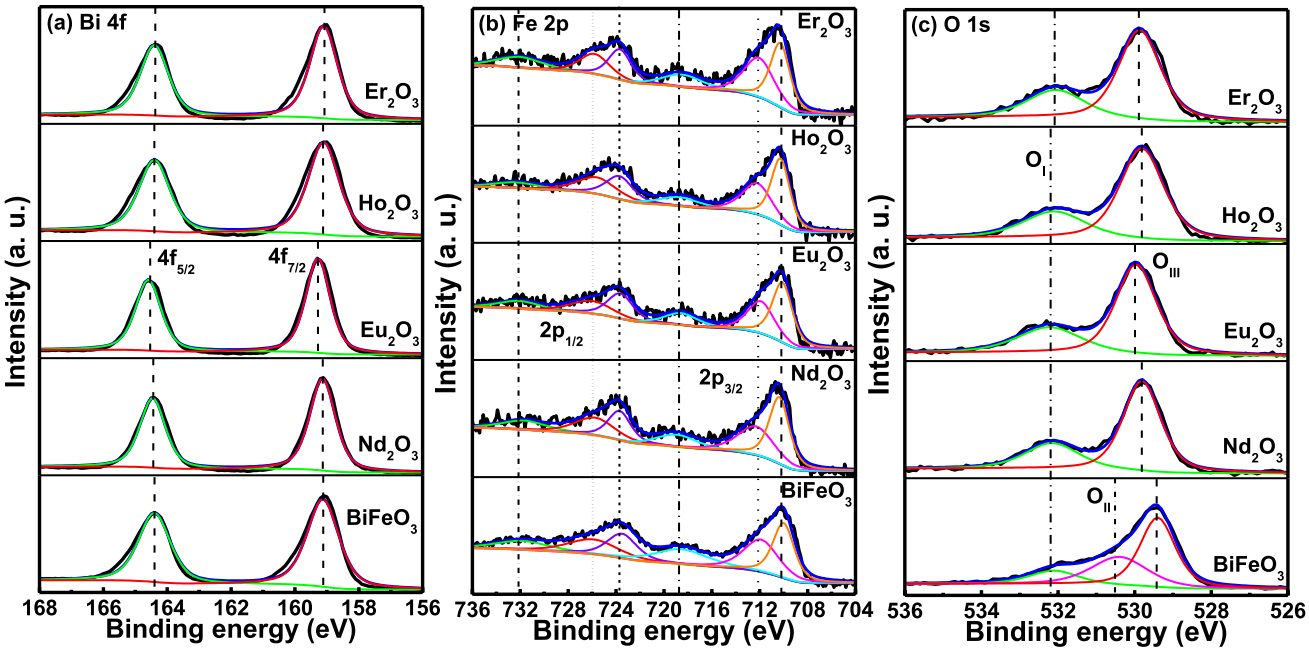

Fig. 5 XPS spectra of **a** Bi 4f, **b** Fe 2p, and **c** O 1 s for $BiFeO_3$ thin film and four different RE_2O_3-buffered $BiFeO_3$ films

three peaks for the $BiFeO_3$ thin film: higher binding (O_I) energy, medium binding (O_{II}) energy, and lower binding (O_{III}) energy. The peaks at 532.2, 530.5, and 529.4 eV were assigned to the chemisorbed oxygen related to the hydroxyl group, oxygen vacancy, and lattice oxygen, respectively [44, 45]. The presence of absorbed water is relevant to the hydroxyl group. However, the $BiFeO_3$ thin films with four RE_2O_3 buffer layers had only two O_I and O_{III} peaks at ~ 532.1 and ~ 529.5 eV, which were associated with lattice oxygen and the hydroxyl group, respectively. The RE_2O_3-buffered sample prevents the creation of oxygen vacancies.

3.2 Ferroelectric characteristics of $BiFeO_3$ capacitive devices with and without RE_2O_3 buffer layers

Figure 6a displays the J-E curves of $BiFeO_3$ capacitive devices with and without RE_2O_3 buffer layers. The control $BiFeO_3$ sample exhibited a measured leakage current density of 2.21×10^{-3} A/cm^2 and 1.45×10^{-2} A/cm^2 at positive and negative applied electric fields of 300 kV/cm, respectively. At the same applied electric field, the RE_2O_3-buffered film showed a significantly reduced leakage current density, at least one order of magnitude lower than that of the control $BiFeO_3$ sample. The main origin of the high leakage current in the $BiFeO_3$ film is believed to be oxygen vacancies resulting from Bi deficiency, fluctuating chemical valence of Fe ion, and different defects including cracks, pores, and interstices [44]. The SIMS data reveals the detection of a depletion layer containing Bi and Fe elements near the surface of the SrRuO3/Si substrate. This occurrence might be attributed to the presence of the capping layer, initially abundant in Bi. Such a layer, potentially comprising secondary phases or defective structures, has the potential to influence the ferroelectric properties of the film. The decrease in leakage current observed in the RE_2O_3-buffered films can be attributed to multiple factors, such as the decrease in Fe valence fluctuation as well as the oxygen vacancies and the inhibition of Bi volatilization caused by the substitution of Bi ions with RE ions. Moreover, the incorporation of RE ions into the $BiFeO_3$ film also contributed to the improvement in surface morphology, resulting in a denser microstructure and fewer interstices, which are favorable for the improvement in leakage current density. Additionally, among the buffer layers, the $BiFeO_3$ film with the Eu_2O_3 buffer layer exhibited the lowest leakage current density of 1.20×10^{-5} A/cm^2 and 2.05×10^{-6} A/cm^2 at 300 kV/cm and − 300 kV/cm, respectively. This outcome may be attributed to the higher Fe^{3+} ion content of the Eu_2O_3-buffered layer, resulting in a smoother surface, reduced volatilization of Bi ions, and stabilization of the hexagonal structure of $BiFeO_3$.

Understanding the leakage current behavior in all samples may require considering various conduction mechanisms such as Schottky emission at the interface, Fowler–Nordheim (FN) tunneling at the interface, space-charge-limited conduction (SCLC), and Poole–Frenkel (FP) emission limited to the bulk. When a positive electric field is applied, the control $BiFeO_3$ sample and RE_2O_3-buffered samples exhibit leakage currents, as shown in Fig. 6b where plotting log(J) versus log(E) suggests SCLC as the dominant leakage current process. At low electric fields, the leakage

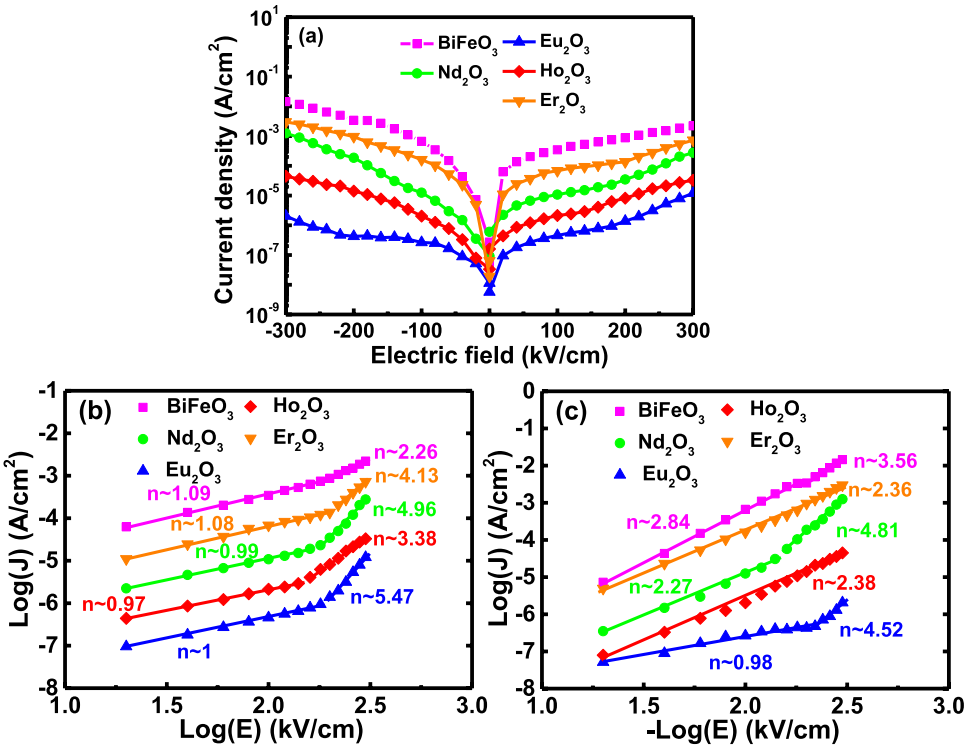

Fig. 6 **a** J-E curves of $BiFeO_3$ capacitive devices with and without four different RE_2O_3 buffer layers. Plots of log(J) versus log (E) for capacitive devices using $BiFeO_3$ thin film and four different RE_2O_3-buffered $BiFeO_3$ films at **b** positive electric field and **c** negative electric field

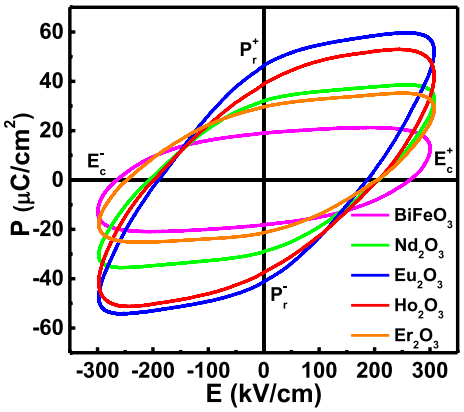

Fig. 7 P-E hysteresis loops of capacitive devices using $BiFeO_3$ thin film and four different RE_2O_3-buffered $BiFeO_3$ films

current behavior of all samples can be explained by Ohmic conduction, while at high electric fields, SCLC is believed to dominate the conduction. Figure 6c shows that SCLC is likely the leakage current mechanism in both $BiFeO_3$ films with and without the RE_2O_3 buffer layer.

At room temperature and 1 kHz, the P-E hysteresis loops of the control $BiFeO_3$ film and RE_2O_3-buffered $BiFeO_3$ films were measured, and the results are presented in Fig. 7. The maximum electric field applied was approximately 300 kV/cm. The P-E loop of the control $BiFeO_3$ thin film had a roundish shape, indicating a high leakage current density. The remanent polarization (P_r) values of the $BiFeO_3$ film without and with the Nd_2O_3, Eu_2O_3, Ho_2O_3, and Er_2O_3 buffer layers were about 18.61, 30.47, 43.76, 38.17, and 25.46 μC/cm^2, respectively, while the coercive field (E_c) values were approximately 264, 207, 188, 203, and 226 kV/cm, respectively. The RE_2O_3 buffer layer significantly improved the ferroelectric behavior of the $BiFeO_3$ thin film by reducing the leakage current density. The Eu_2O_3-buffered layer showed the lowest coercive field and the largest remanent polarization among the RE_2O_3 buffer layers. The increase in polarization for the Eu_2O_3-buffered layer was attributed to the lowest current density and the highest degree of (110)-preferred orientation.

4 Conclusion

A comprehensive series of experiments was undertaken to explore the characteristics of $BiFeO_3$ thin films, each featuring a unique RE_2O_3 buffer layer. These films were fabricated through a simple spin-coating method on $SrRuO_3/n^+$-Si substrates. Examination of XRD data confirmed a distinct (110) preferred orientation within the RE_2O_3 buffer layer, free from any impurities or secondary phases. This finding was reinforced by SIMS depth profiling, which revealed a substantial concentration of RE ions within the $BiFeO_3$ film. Additionally, AFM imaging revealed the smooth surface of the RE_2O_3 buffer layer, adorned with small, flake-like structures free of any cracks. Further analysis using XPS demonstrated a notable Fe^{3+}/Fe^{2+} ratio and a suppression of oxygen

vacancies in the RE_2O_3 buffer layers. These structural attributes were found to have a direct correlation with the ferroelectric properties of the $BiFeO_3$ thin films. Remarkably, the films featuring RE_2O_3 buffer layers exhibited superior electrical characteristics compared to the control film. Notably, the Eu_2O_3 buffer layer demonstrated exceptional performance, boasting the lowest leakage current of 2.05×10^{-6} A/cm^2, the highest remnant polarization of 43.76 μC/cm^2, and the smallest coercive field of 188 kV/cm. These outstanding attributes stem from a combination of factors, including low surface roughness, robust (110) orientation, increased Fe^{3+} content, and minimized oxygen vacancies. Consequently, the Eu_2O_3 buffer layer holds significant promise for enhancing the ferroelectric properties of $BiFeO_3$ thin films, making them highly suitable for a diverse range of multifunctional applications.

Acknowledgements The authors would like to thank their appreciation to the entire staff of the Thin Film Measurement Lab, Chang Gung University for their technical help. This work was supported by Ministry of Science and Technology (MOST) of Taiwan under contract of MOST 109-2221-E-182-028.

Author contributions All authors contributed to the study conception and design. Material preparation, data collection, and analysis were performed by TM, ZY and JL. TM and ZY contributed significantly to analysis and manuscript preparation. The first draft of the manuscript was written by TM. All authors read and approved the final manuscript.

Data availability The data presented in this study are available on request from the corresponding author.

Declarations

Conflict of interest The authors declare that they have no conflict of interest.

References

1. A. Billah, Y. Matsuno, A.N. Anju, K. Koike, S. Kubota, F. Hirose, B. Ahmmad, Unusual behavior of magnetic coercive fields with temperature and applied field in La-doped $BiFeO_3$ ceramics. ACS Appl. Electron. Mater. **5**, 4261–4267 (2023)
2. R.S. Viswajit, K. Ashok, K.B. Jinesh, Tailoring of charge carriers with deposition temperature in pulsed laser deposited $BiFeO_3$ thin films. Appl. Surf. Sci. **661**, 160016 (2024)
3. S. Ratha, M. Kuppan, G. Egawa, S. Yoshimura, Excellent magnetic properties in multiferroic $BiFeO_3$ based thin films for magnetic devices application. Nano-Struct. Nano-Objects **35**, 101007 (2023)
4. X. Gao, L. Dai, Y. Liu, K. Wang, D.V. Karpinsky, L. Liu, Y. Wang, Reliable ferroelectricity in sol–gel-derived $BiFeO_3$ thin films below 200 nm. J. Am. Ceram. Soc. **107**, 3301–3312 (2024)
5. E. Hannachi, M.I. Sayyed, K.A. Mahmoud, Y. Slimani, S. Akhtar, B. Albarzan, A.H. Almuqrin, Impact of tin oxide on the structural features and radiation shielding response of some ABO_3 perovskites ceramics (A = Ca, Sr, Ba; B = Ti). Appl. Phys. A **127**, 970 (2021)
6. M. Reda, E.E. Ateia, S.I. El-Dek, M.M. Arman, New insights into optical properties, and applications of Zr-doped $BaTiO_3$. Appl. Phys. A **130**, 240 (2024)
7. T.-M. Pan, H.-C. Wang, J.-L. Her, Structural and electrical characteristics of high-performance stacked $YbTi_xO_y/PbZr_{0.53}Ti_{0.47}O_3$ gate dielectrics for InGaZnO thin-film transistors. J. Alloys Compd. **842**, 155844 (2020)
8. M. Sk, Recent progress of lead-free halide double perovskites for green energy and other applications. Appl. Phys. A **128**, 462 (2022)
9. S. Supriya, Crystal structure engineered non-toxic $Bi_{0.5}Na_{0.5}TiO_3$ based thin films- fabrication process, enhanced electrical performance, challenges and recent reports. J. Inorg. Organomet. Polym. Mater. **33**, 3013–3026 (2023)
10. S. Supriya, Electric field assisted spark plasma sintering of ABO_3 perovskites: crystal structure, dielectric behavior and future challenges, open ceramics. Open Ceramics **18**, 100608 (2024)
11. L. You, A. Abdelsamie, Y. Zhou, L. Chang, Z.S. Lim, J. Wang, Revisiting the ferroelectric photovoltaic properties of vertical $BiFeO_3$ capacitors: a comprehensive study. ACS Appl. Mater. Interfaces **15**, 12070–12077 (2023)
12. X. Tan, X. Sun, J. Jiang, D. Chen, Improved polarization retention in epitaxial $BiFeO_3$ thin films induced by strain relaxation. Appl. Surf. Sci. **635**, 157703 (2023)
13. Z. Wang, X. Yang, X. He, H. Xue, X. Wang, H. Dong, J. Zhu, W. Mao, X. Xu, X. Li, Roles of oxygen vacancy and ferroelectric polarization in photovoltaic effects of $BiFeO_3$ based devices. Solid State Commun. **360**, 115042 (2023)
14. P. Ravindran, R. Vidya, A. Kjekshus, H. Fjellvåg, Theoretical investigation of magnetoelectric behavior in $BiFeO_3$. Phys. Rev. B **74**, 224412 (2006)
15. F. Kubel, H. Schmid, Structure of a ferroelectric and ferroelastic monodomain crystal of the perovskite $BiFeO_3$. Acta Crystallogr. B **46**, 698–702 (1990)
16. H.W. Shin, J.Y. Son, Leakage current characteristics of polycrystalline $BiFeO_3$ thin films affected by thickness-dependent domain wall currents. J. Alloys Compd. **968**, 172113 (2023)
17. T. Ahmad, K. Jindal, M. Tomar, P.K. Jha, Effect of codoping of rare earth elements and Cr on multiferroic, optical and photocatalytic properties of $BiFeO_3$. Mater. Today Commun. **37**, 107516 (2023)
18. S. Kumari, K. Anand, M. Alam, L. Ghosh, S. Dixit, R. Singh, A.K. Jain, S.M. Yusuf, C. Gautam, A.K. Ghosh, A. Mohan, S. Chatterjee, Enhancement of multiferroic and optical properties in $BiFeO_3$ due to different exchange interactions between transition and rare earth ions. Phys. Status Solidi B **260**, 2300026 (2023)
19. Y. Xu, C. Deng, X. Wang, Bandgap modulation and phase boundary region of multiferroic Gd, Co co-doped $BiFeO_3$ thin film. AIP Adv. **13**, 115004 (2023)
20. W. Mao, Q. Yao, Y. Fan, Y. Wang, X. Wang, Y. Pu, X. Li, Combined experimental and theoretical investigation on modulation of multiferroic properties in $BiFeO_3$ ceramics induced by Dy and transition metals co-doping. J. Alloys Compd. **784**, 117–124 (2019)
21. D.V. Karpinsky, A. Pakalniškis, G. Niaura, D.V. Zhaludkevich, A.L. Zhaludkevich, S.I. Latushka, M. Silibin, M. Serdechnova, V.M. Garamus, A. Lukowiak, W. Stręk, M. Kaya, R. Skaudžius, A. Kareiva, Evolution of the crystal structure and magnetic properties of Sm-doped $BiFeO_3$ ceramics across the phase boundary region. Ceram. Int. **47**, 5399 (2021)
22. M.S. Bernardo, Synthesis, microstructure and properties of $BiFeO_3$-based multiferroic materials: a review. Bol. Soc. Esp. Ceram. Vidr. **53**, 1 (2014)
23. J.A. Boukhari, A. Khalaf, R.S. Hassan, R. Awad, Structural, optical and magnetic properties of pure and rare earth-doped NiO nanoparticles. Appl. Phys. A **126**, 323 (2020)

24. S. Supriya, Effect of doping and enhanced microstructures of bismuth titanates as aurivillius perovskites. Micron **162**, 103344 (2022)
25. S. Supriya, Research progress, doping strategies and dielectric-ferroelectric anomalies of rare earth-based $Bi_{0.5}Na_{0.5}TiO_3$ perovskites. J. Rare Earths (2024). https://doi.org/10.1016/j.jre.2023.10.009
26. S. Supriya, Tailoring layered structure of bismuth-based aurivillius perovskites: recent advances and future aspects. Coord. Chem. Rev. **479**, 215010 (2023)
27. K.S.K.R.C. Sekhar, T. Patri, A.M. Tighezza, D.S. Saini, P. Rosaiah, A. Ghosh, Dielectric relaxation and electrical conductivity property correlation in Gd-doped BBTO Aurivillius ceramics. Appl. Phys. A **130**, 150 (2024)
28. R.Y. Zheng, C.H. Sim, J. Wang, S. Ramakrishna, Effects of SRO buffer layer on multiferroic $BiFeO_3$ thin films. J. Am. Ceram. Soc. **91**, 3240–3244 (2008)
29. C.-C. Leu, T.-J. Lin, S.-Y. Chen, C.-T. Hu, Effects of bismuth oxide buffer layer on $BiFeO_3$ thin film. J. Am. Ceram. Soc. **98**, 724–731 (2014)
30. W. Tang, J. Yang, J. Zhang, Y. Jiang, J. Wang, L. Cao, Y. Fu, Write-once-read-many-times memory device based on Pt/$BiFeO_3$/$LaNiO_3$ heterostructures. Appl. Surf. Sci. **618**, 156591 (2023)
31. Q. Cao, Y. Zhao, R. Ye, X. Chen, X. Hu, N. Zhuang, Piezoelectric and magneto-optical effect of lanthanum-doped bismuth ferrite films on silicon substrate. J. Alloys Compd. **967**, 171840 (2023)
32. Y.J. Acosta-Silva, L.A. Godínez, M. Toledano-Ayala, R. Lozada-Morales, O. Zelaya-Angel, A. Méndez-López, Study of the effects of Er doping on the physical properties of CdSe thin film. Magnetochemistry **9**, 107 (2013)
33. Y.J. Acosta-Silva, A. Méndez-López, F. de Moure-Flores, S. Tomás, R. Lozada-Morales, M. Meléndez-Lira, O. Zelaya-Angel, Characterization of substitutional and interstitial Eu^{+3}-positions in CdS lattice. Mater. Chem. Phys. **257**, 123763 (2021)
34. N.V. Giridharan, S. Supriya, Effect of processing on the properties of $Bi_{3.15}Nd_{0.85}Ti_3O_{12}$ thin films. Thin Solid Films **516**, 5244–5247 (2008)
35. S. Supriya, A review on lead-free-$Bi_{0.5}Na_{0.5}TiO_3$ based ceramics and films: dielectric, piezoelectric, ferroelectric and energy storage performance. J. Inorg. Organomet. Polym. Mater. **32**, 3649–3676 (2022)
36. S.R.A. Ahmed, Structural and electrical behaviors of silicon nitride thin-films deposited using spin coating technique. Appl. Phys. A **129**, 504 (2023)
37. P. Suresh, S. Srinath, Effect of synthesis route on the multiferroic properties of $BiFeO_3$: a comparative study between solid state and sol–gel methods. J. Alloys Compd. **649**, 843–850 (2015)
38. S. Sharma, V. Singh, R.K. Kotnala, R.K. Dwivedi, Comparative studies of pure $BiFeO_3$ prepared by sol–gel versus conventional solid-state-reaction method. J. Mater. Sci. Mater. Electron. **25**, 1915–1921 (2014)
39. R. Zheng, X. Gao, J. Wang, Multiferroic $BiFeO_3$ thin films buffered by a $SrRuO_3$ layer. J. Am. Ceram. Soc. **91**, 463–466 (2008)
40. J. Wu, J. Wang, $BiFeO_3$ thin films of (111)-orientation deposited on $SrRuO_3$ buffered Pt/TiO_2/SiO_2/Si(100) substrates. Acta Mater. **58**, 1688–1697 (2010)
41. R.D. Shannon, Revised effective ionic radii and systematic studies of interatomic distances in halides and chalcogenides. Acta Crystallogr. **32**, 751–767 (1976)
42. C.-C. Leu, T.-J. Lin, S.-Y. Chen, C.-T. Hu, Effects of bismuth oxide buffer layer on $BiFeO_3$ thin film. J. Am. Ceram. Soc. **98**, 724–731 (2015)
43. S. Chauhan, M. Kumar, S. Chhoker, S.C. Katyal, M. Jewariya, B.N. Suma, G. Kunte, Structural modification and enhanced magnetic properties with two phonon modes in Ca–Co codoped $BiFeO_3$ nanoparticles. Ceram. Int. **41**, 14306–14314 (2015)
44. F. Lin, Q. Yu, L. Deng, Z. Zhang, X. He, A. Liu, W. Shi, Effect of La/Cr codoping on structural transformation, leakage, dielectric and magnetic properties of $BiFeO_3$ ceramics. J. Mater. Sci. **52**, 7118–7129 (2017)
45. Y.-H. Si, Y. Xia, S.-K. Shang, X.-B. Xiong, X.-R. Zeng, J. Zhou, Y.-Y. Li, Enhanced visible light driven photocatalytic behavior of $BiFeO_3$/reduced graphene oxide composites. Nanomaterials **8**, 526 (2018)